Chapter 6 : High Frequency Phantom Characterization

Next, we describe methods to characterize the acoustic properties of high-frequency reference phantoms that are necessary to generate parametric imaging based on quantitative ultrasound features with the reference phantom method. Recently, Madsen et al. [1] developed tissue-mimicking (TM) phantoms with ultrasonic properties of human arteries at very high frequencies [2]. Accurate characterization of the acoustic properties of these new phantoms poses additional challenges relative to the same characterization at lower frequencies. In this chapter, we describe the methods applied to characterization of these phantoms. Methods to determine the attenuation coefficient, phase velocity, and absolute backscatter coefficient are described. [1]

1 This chapter is adapted from McCormick, M, Madsen, E., Deaner, M., and Varghese, T. *Absolute Backscatter Coefficient Estimates of Tissue-Mimicking Phantoms in the 5-50 MHz Frequency Range*. Journal of the Acoustical Society of America. In Review.

6.1 Tissue-mimicking phantoms

The TM phantoms examined in this chapter are produced as reference phantoms for use at high frequencies [1]. Each phantom is macroscopically uniform. The base material of the phantoms consists of a mixture of agarose, propylene glycol, Germall Plus (preservative), and ultra-filtered whole bovine milk. Scattering is due to randomly distributed glass beads. Two phantoms are examined with different glass bead concentrations (mass per unit volume) and different diameter distributions (catalog numbers 4000E and 5000E, Potter Industries, Inc., Valley Forge, Pennsylvania, USA). The two phantoms will henceforth be referenced as the '4000E phantom' and '5000E phantom', respectively. The diameter distributions of the two glass bead categories that are utilized in these phantoms are shown in Fig. 6.1; mean scatterer diameters of the 4000E and 5000E phantoms are 5.40 μm and 5.16 μm, respectively. The diameters are measured by placing beads in an agarose suspension and viewing under an optical microscope. Approximately 500 diameter measurements are made for each bead source. The diameter percentage is calculated by binning the measurements and dividing by the total frequency. The percentage is also calculated with the kernel density estimation (KDE) technique [3, 4]; a Gaussian kernel is used with bandwidth automatically calculated using the method of Silverman [5]. The concentration of the 4000E bead is 6.00 g/L, and that of the 5000E beads is 15.60 g/L.

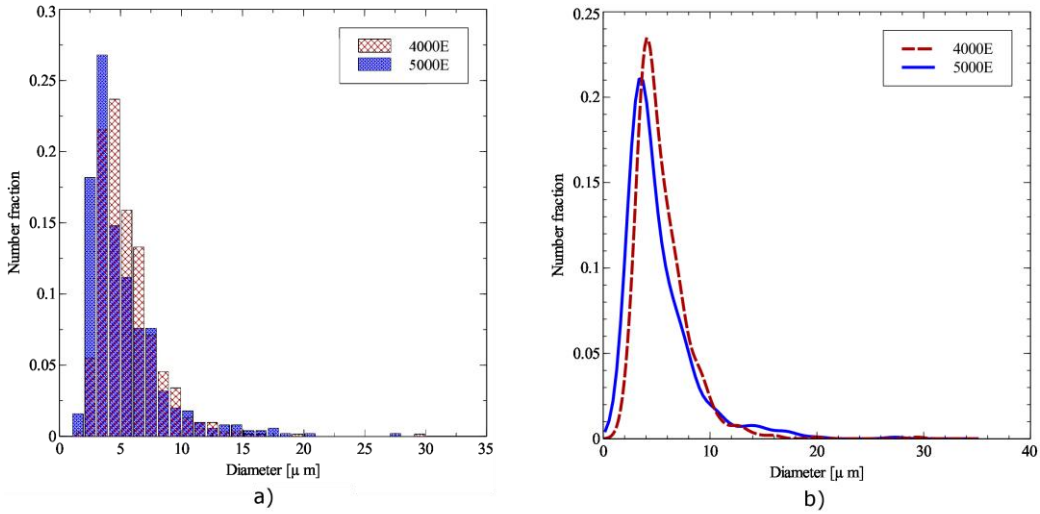

Figure 6.1: Size distribution of the TM phantom glass bead scatterers. a) 4000E and 5000E distribution determined with a histogram divided by the total frequency. b) 4000E and 5000E distribution determined with the KDE method.

6.2 Attenuation characterization

Attenuation is measured with the standard narrowband substitution technique [6, 7]. Attenuation, the rate of decrease in amplitude with depth, *z* of the amplitude, *A*, of an pressure pulse is assumed to be linearly proportional to the amplitude of the pulse,

$$\frac{dA}{dz} = -\alpha A$$

Eqn. 6.1

where α denotes the attenuation coefficient. The amplitude of the acoustic wave decreases exponentially with time,

$$A(t) = A_0 \exp(-\alpha z)$$

Eqn. 6.2

if A_0 is the initial wave amplitude.

To measure the attenuation coefficient with the substitution method, we measure the wave amplitude in a water-only path and after insertion of a TM sample with known thickness. Taking the ratio of the equation in both situations allows us to remove the A_0 constant and solve for the attenuation coefficient.

Figure 6.2: Water tank with experimental apparatus for the narrowband substitution technique. The transducers are suspended in the tank by a system of mounts with translational and rotational degrees of freedom. A heater keeps the water at a constant 22.0º C. For calculation of both the phase velocity and

the attenuation coefficient, signal is collected from a water-only path (shown), and with the sample placed in the path of the transducers (not shown). A function generator and pulse amplifier provide input to the transmitting transducer, and the oscilloscope and computer are to record the received signal.

The experimental apparatus layout is illustrated in Fig. 6.2. The water tank is filled with degassed, reverse osmosis water to provide a medium for ultrasound propagation. Since the acoustic properties of water, in particular the sound speed, can change with temperature, the tank water is kept at a controlled 22.0 °C by a Haake DC10 heater (Thermo Fisher Scientific Inc.). Especially at high frequencies, it is important to temporarily turn off the circulating heater during signal acquisition to reduce vibrations that would impact time delays and cause jitter while averaging sweeps. For the same reasons, it is critical to ensure the experimenter does not make contact with the water tank while data is collected.

A Wavetek model 81 Function Generator is set to burst mode to generate a sinusoid tone burst of 30 wavelengths. In the *narrowband* substitution method, measurements are made independently at individual frequencies. The narrowband measurement frequency is the frequency of the sine waves in the tone burst. While a theoretical narrowband input would be a continuous sinusoid for all time, the signal can effectively be considered narrow band near the center of the tone burst where edge effects decrease to negligible levels. The use of a tone burst instead of a continuous wave is required for two reasons: the transducers have a limited power dissipation capacity, and the start of the burst serves as a fiducial marker when determined delays for speed of sound calculations. The input function generator signal is amplified by a model 75A250A radiofrequency (RF) amplifier (Amplifier Research, Souderton, PA, USA) to provide a high voltage excitation of the ultrasound transducers.

A sealed, co-axial BNC (Bayonet Neill-Concelman) connection to the transducers is made to the transducers. The signal is transmitted and received by a V358 50 MHz center frequency

unfocused transducer pair (Olympus Panametrics-NDT, Waltham, MA, USA). The transducers are aligned by peaking the received signal with a micrometer controlled translation unit (Ardel Kinematic Inc., Stratford, CT, USA) and gimbal mount (Newport Oriel, Stratford, CT, USA). The transducers are separated by a relatively close 42 μs delay (62.5 mm signal propagation path) to prevent attenuation of the signal. These transducers, serial numbers 630314 and 630315, are well matched in their spectral response with a -6 dB bandwidth from 28 MHz to 65 MHz as shown in Fig. 6.3. In practice we find that sufficient signal can be obtained from 10 MHz to 70 MHz.

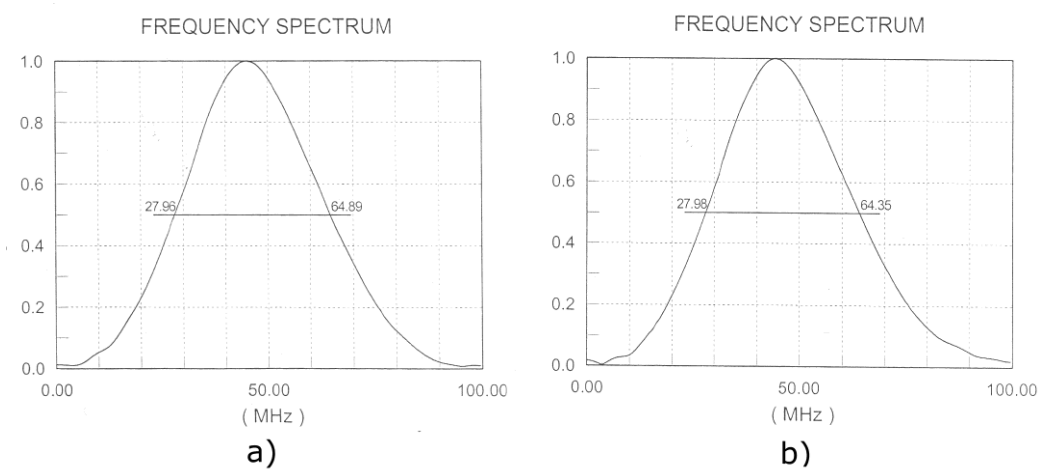

Figure 6.3: Impulse response of the two transducers, serial number 630314 and 630315, used to measure the sound speed and attenuation of the phantom sample. Measurements are provided by Olympus Panametrics-NDT and performed per ASTM E1065.

The received signal is digitized and displayed with the WaveRunner LT342 oscilloscope (LeCroy, Chestnut Ridge, NY, USA). The received signal was collected at 500 MS/s, and ten independent sets of 100 averaged pulses were transferred to a computer for further offline analysis.

Vibration from the buildings or other sources can cause jitter in received waveform, which

will decrease the averaged amplitude. A guard against this source of error is to plot the waveform before and after averaging, as in Fig. 6.4.

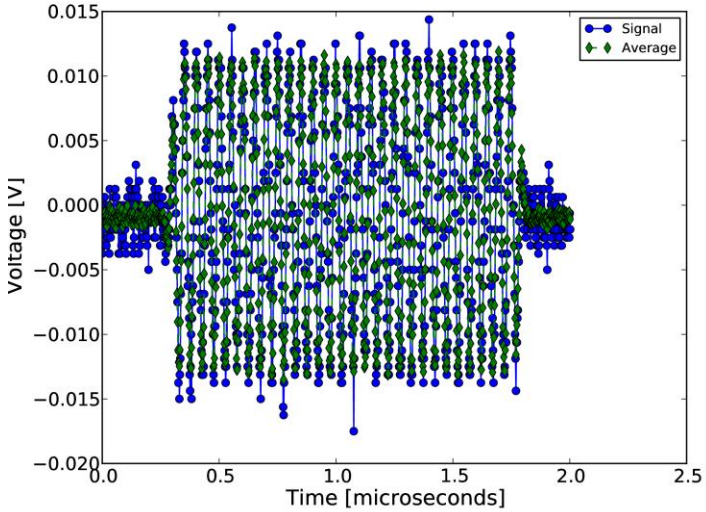

Figure 6.4: Received waveform from the 5000E sample before and after averaging. Noise is removed from averaged waveform, but the amplitude does not decrease, which can occur when jitter is present.

Frequency-dependent attenuation causes distortion at the beginning and the end of the tone burst. In order to ensure that we are measuring the amplitude at the narrowband portion of the signal, we calculate the root-mean-square amplitude where correlation with a 20 cycle sine wave of the excitation wave is peaked. If the received signal is viewed in the time-frequency plane, only the central portion of the tone burst is effectively narrowband. As shown in Fig. 6.5c) and Fig. 6.5d), the edges of the signal, which have lower local frequency content, experience less attenuation. A spectrogram, Fig. 6.6, demonstrates that in a frequency-time plane, the power spectral density of the signal is narrowband only at the center of the tone burst.

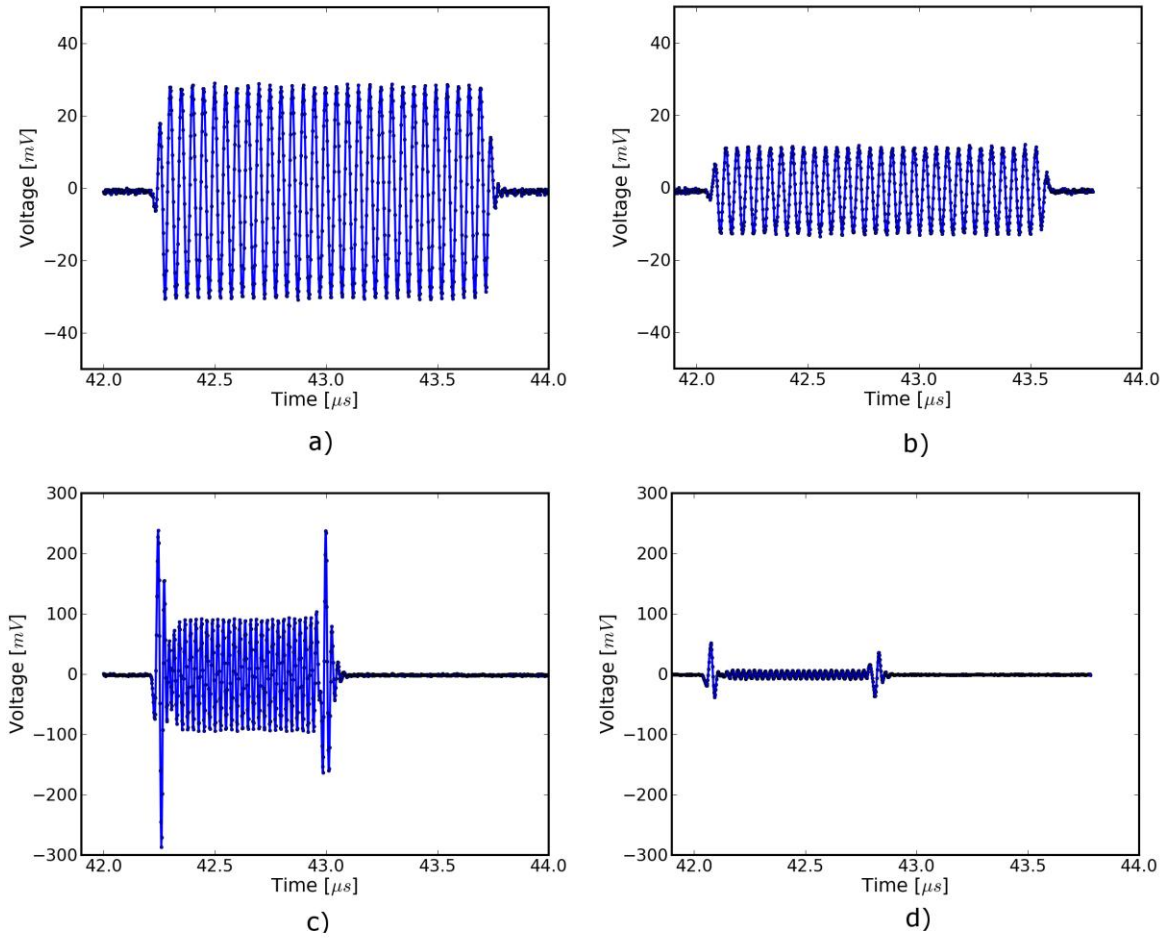

Figure 6.5: Averaged, received signals obtained using the narrowband substitution method. a) water-only signal at 20 MHz, b) 5 mm sample inserted with the center frequency at 20 MHz, c) water-only signal at 40 MHz, and d) sample inserted with the center frequency at 40 MHz. Time is relative to excitation at the source transducer and the plotted time axes limits are kept consistent to demonstrate time shifts. Amplitudes are kept consistent at each frequency, but the excitation amplitude is adjusted with frequency so sufficient signal-to-noise ratio is obtained without saturation and non-linear propagation. The dramatic effect of frequency-dependent attenuation on the signal shape can be seen in d).

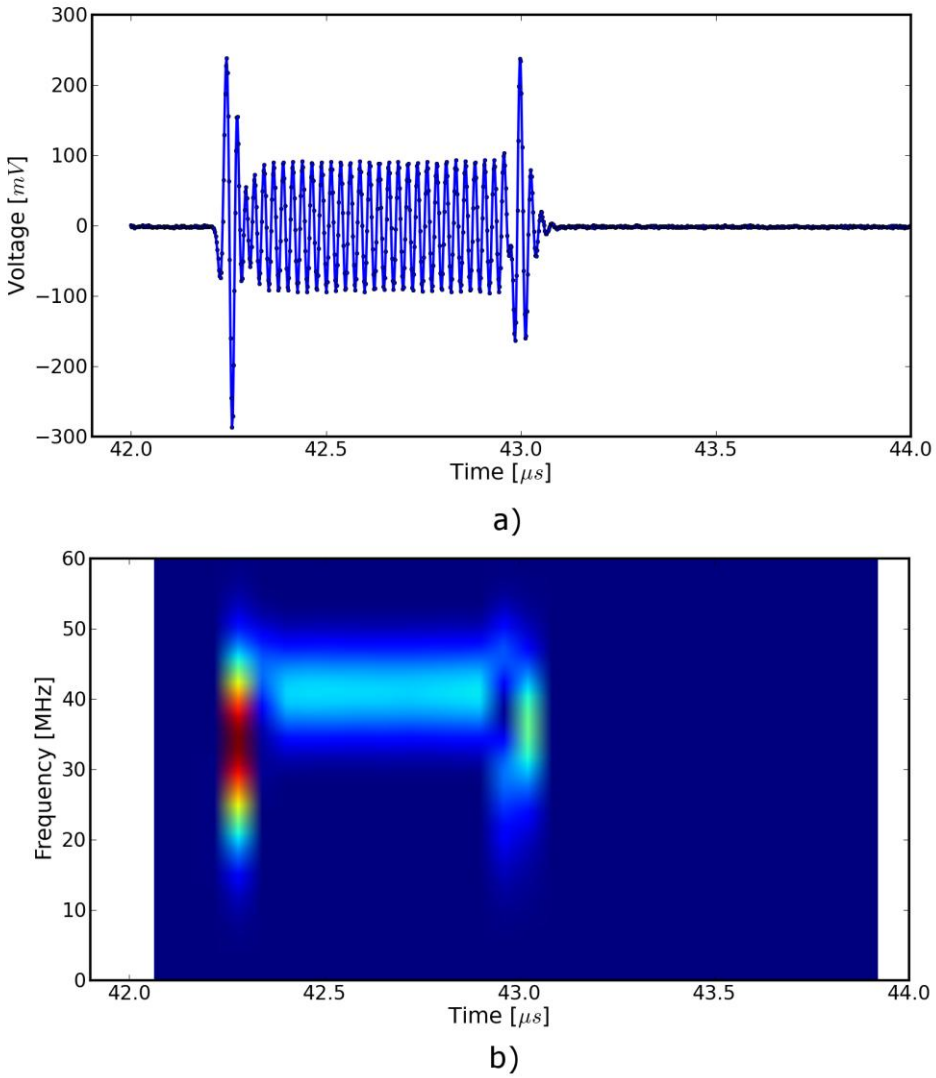

Figure 6.6: Spectrogram of the water-only signal at 40 MHz. a) Signal amplitude versus time. b) Spectrogram where the power spectral density is mapped to colors and shown over the same time period. A moving Hanning window of 64 points is used to calculate the power spectral density with an overlap of 32 points and zero-padding to 512 points. The signal is only narrow-band around 40 MHz at the center of the tone burst.

When sound is transmitted through the water-only path, its amplitude decreases across z_1, the distance from the transmitting transducer to where the start of the sample will be placed, across d, the thickness of the sample, and z_2, the distance from the end of the sample to

receiving transducer.

$$A_w = A_0 \exp(-\alpha_w z_1) \exp(-\alpha_w d) \exp(-\alpha_w z_2)$$

Eqn. 6.3

When sound propagates through the surrounding water and sample, the received amplitude is,

$$A_s = A_0 \exp(-\alpha_w z_1) T \exp(-\alpha_s d) \exp(-\alpha_w z_2)$$

where *T* is the total transmission coefficient of the two thin films enclosing the sample. When constructing the substitution method sample, the material used is the same as that produced during creation of the backscatter phantom but is covered by 12.2 μm thick Saran Wrap® film inside an acrylic cylinder. The transmission coefficient, while nearly constant at lower frequencies, deviates at high frequencies, as shown in Fig. 6.7. The transmission coefficient, *T*, is given by [8]

$$\left|\frac{2Z_s}{(Z_w + Z_s)\cos((\frac{2\pi f}{c_{Saran}} - j\alpha(f))l) + j(Z_{Saran} + \frac{Z_w Z_s}{Z_{Saran}})\sin((\frac{2\pi f}{c_{Saran}} - j\alpha(f))l)}\right| \times \left|\frac{2Z_w}{(Z_s + Z_w)\cos((\frac{2\pi f}{c_{Saran}} - j\alpha(f))l) + j(Z_{Saran} + \frac{Z_s Z_w}{Z_{Saran}})\sin((\frac{2\pi f}{c_{Saran}} - j\alpha(f))l)}\right|$$

Eqn. 6.4

where Z_w, Z_s, and Z_{Saran}, are the acoustic impedances of water, the sample, and Saran Wrap respectively, *f* is the frequency, c_{Saran} is the speed of sound in Saran, *α(f)* is the attenuation coefficient of the Saran Wrap in *Np/m*, and *l* is the thickness of each thin layer. In our case c_{Saran}

is 2400 *m/s*, $\alpha(f)[Np/m] = 5.0\, f^{1.5}$, the Saran density, ρ_{Saran} is 1.69 *g/mL*. Thickness of the Saran Wrap, which was 25 μm in previous cases, is re-measured, and the other properties, are assumed to be the same as those fit in Wear et al. [8]. Acoustic impedance, *Z*, for a material is the product of its density and speed of sound. The density of the TM material was 1.045 g/mL for the 4000E phantom and 1.062 g/mL for the 5000E phantom. Methods to obtain values for speed of sound of the test materials used in the attenuation coefficient calculation are described in the next section.

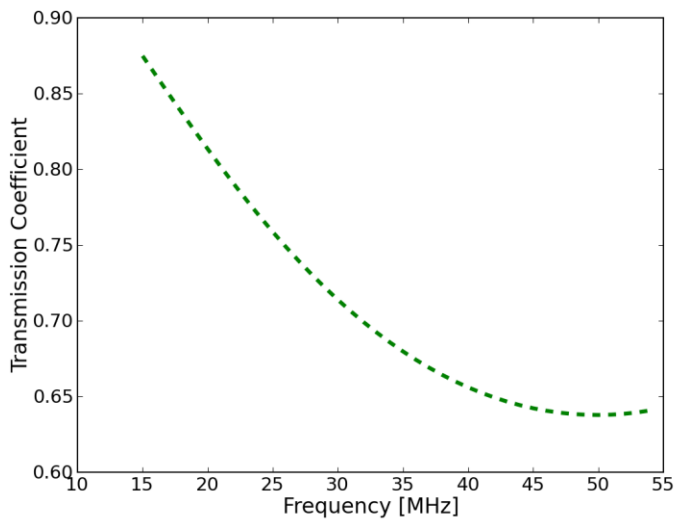

Figure 6.7: Transmission coefficient of the two thin Saran Wrap layers covering the production sample used in attenuation estimation experiments. Note the dependence on frequency.

Again, the attenuation coefficient, α, in dB/cm is calculated using the signal amplitude in the absence of the sample, A_w, the signal amplitude with the sample in place, A_s. Taking the two equations that define the attenuation in water-only and water-with-sample cases and dividing them, solving for α, and placing the result in decibels per centimeter, we obtain:

$$\alpha(f) = \frac{20}{d}\log_{10}(\frac{A_w T_{total}}{A_s}) + \alpha_w(f)$$

Eqn. 6.5

The thickness of the test cylinder is 5.00 mm as measured with a calibrated micrometer. This is significantly thinner than the larger 'hockey-puck' cylinders used at lower frequencies to limit high frequency attenuation.

Attenuation of water, α_w, which is negligible at lower frequencies, must be accounted for at high frequencies. Attenuation of water is proportional to the square of frequency from 3-70 MHz [9], and in dB/cm is

$$\alpha_w(f)[dB/cm] = 2.08e^{-3} f^2$$

Eqn. 6.6

when *f* is in MHz.

Results of attenuation coefficient characterization for both the 4000E and 5000E phantom is shown in Fig. 6.8. Values from fitting to a power law model

$$\alpha(f)[dB/cm] = \alpha_0 f^n$$

Eqn. 6.7

are tabulated in Table 6.1.

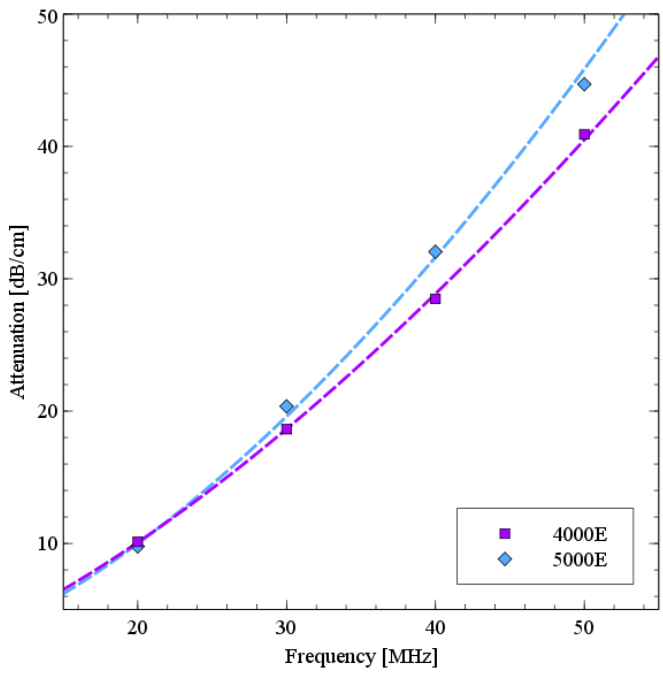

Figure 6.8: Measured attenuation for the 4000E phantom and 5000E phantom. Dashed lines show the results of fitting to a power law model.

TM phantom	α_0 [dB/cm]	n	Coefficient of determination (R^2)
4000E	0.107	1.52	0.9997
5000E	0.069	1.66	0.9979

Table 6.1: Parameters for a power law fit to the TM phantom attenuations.

6.3 Phase velocity characterization

Speed of sound is another fundamental acoustic property. Tissue vary to some degree; for instance, fat has a lower sound speed (1478 m/s) and tendon has a higher sound speed (1670 m/s) [10]. However, the canonical sound speed assumed by clinical scanners for soft tissues is 1540 m/s.

The speed of sound is then obtained by inserting the change in time delay, Δ*t*, and sample

thickness, *d*, into the following equation [11]

$$c = \frac{c_w}{1 + \frac{c_w \Delta t}{d}}$$

Eqn. 6.8

if Δ*t* is the difference in the time delay between water-with-sample and water-only cases, t_w - t_s. The speed of sound in pure water, c_w, at 22º C is 1488.3 m/s [12].

Considerable changes in the shape of the pulse occur because of frequency dependent attenuation (see Fig. 6.5). As with the attenuation coefficient, this poses challenges to measuring the quantity needed to calculate the speed of sound, the time delay of a tone burst. When measuring the delay of a pulse or tone burst, there are different velocity definitions depending on how the delay is defined. The *signal velocity* results from measuring the delay of the front of a pulse, *group velocity* from the center of a pulse, and *phase velocity* if the delay of a single frequency component is measured [11]. The phase velocity is the most desirable because signal velocity and group velocity have broad spectral content. In general there is dispersion in phase velocity, so it is difficult to apply signal or group velocity results to other situations where the spectral content differs.

To precisely obtain the phase velocity, the same narrowband pulse zero-crossing location is found in the tone burst of the water-only signal and the water-with-sample signal. First, we find the delay to a zero-crossing at the center of the water-only tone burst. To locate this zero-crossing, we first find the 'start' of the received tone burst. The 'start' of the tone is where the signal exceeds the electronic noise that comes before the tone burst. The noise level is quantified by measuring the standard deviation of the first 100 samples of the received waveform. The start

of the signal is taken as the sample where the received signal exceeds eight times the noise standard deviation. An approximate center of the pulse is found by moving 15 periods past the start. The closest zero-crossing is linearly interpolated from the samples to obtain a precise delay for the water-only signal. The procedure is repeated for the water-with-sample signal, but instead of moving 15 periods past the start, the offset is the closest zero-crossing to the difference between the water-only zero-crossing and the water-only start. This ensures the same relative zero-crossing in the tone burst is used as the delay for both the water-only and the water-with-sample cases. This will be true as long as the distortion at the front edge of the signal does not approach half a period, which has empirically proven to be a valid assumption. Figure 6.9 shows the delay samples selected in this process at 50.0 MHz for the water-only signal and after the 5000E signal is inserted.

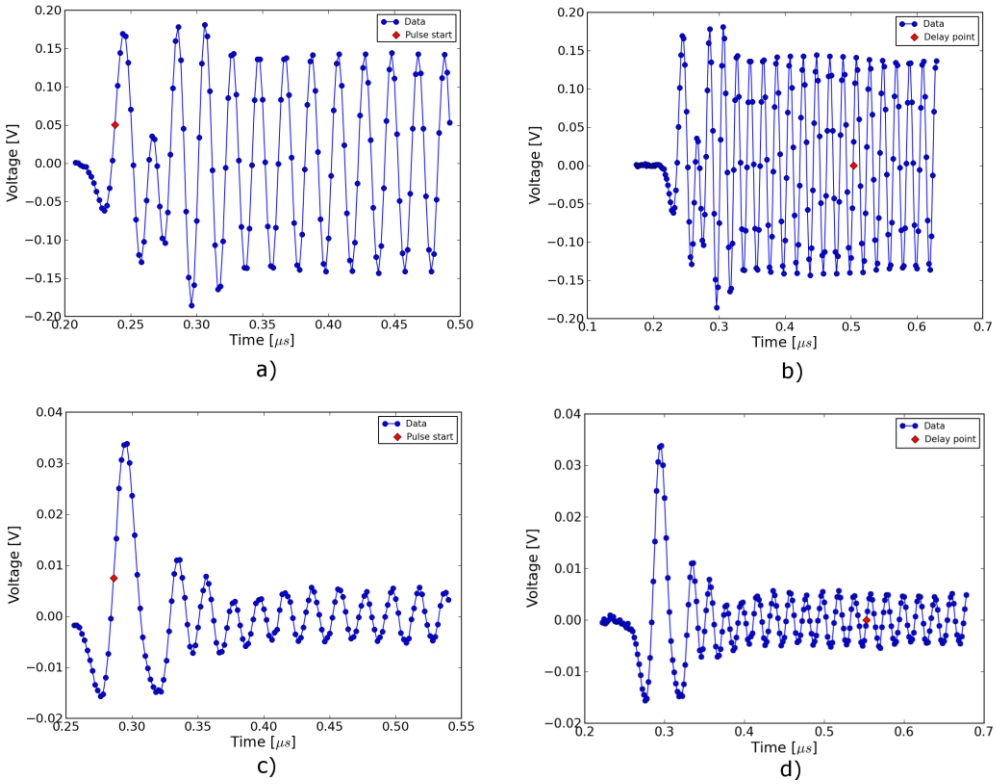

Figure 6.9: Delay samples used in phase velocity calculations. Measurements made at 50 MHz. An offset from the water signal start sample, a), to a zero-crossing at the center of the water-only tone burst, b), is used to find the corresponding zero-crossing, d), given the water-with-sample start, c).

An alternative method to the above is to take the delay to be the lag to the maximum of the cross-correlation of the two signals. A more precise location of the cross-correlation peak can be obtained with parabolic interpolation of the peak. Of course, the broad-band edges of the tone burst are included in the cross-correlation calculation. Results for both methods are shown in Fig. 6.10. The calculated phase velocities are similar, but the zero-crossing method trend is closer the expected dispersion. According to the Kramers-Krönig relations [13, 14], increased attenuation with frequency will cause an increase in phase velocity with frequency. Since attenuation increases monotonically with frequency, it is expected that phase velocity will

increase monotonically with frequency. Although, the observed dispersion is minute compared to the variation found in soft tissues. The phase velocity for both phantoms at 30 MHz is shown in Table 6.2.

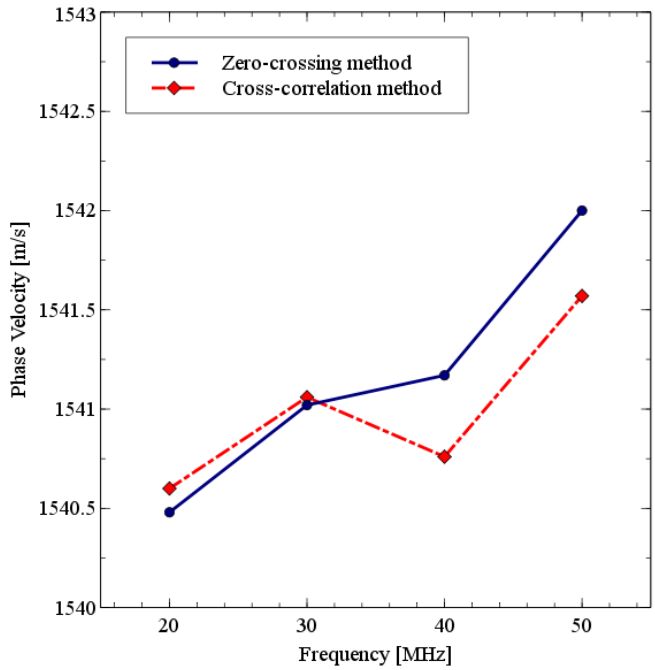

Figure 6.10: Phase velocity for the 5000E phantom calculated when the delay is determined with two different methods: zero-crossing in the narrowband portion of the signal, and lag of the cross-correlation peak.

TM phantom	Phase velocity [m/s]
4000E	1541.02
5000E	1540.64

Table 6.2: Phase velocity for the phantoms characterized at 30 MHz calculated with the narrowband zero-crossing method.

6.4 Absolute backscatter estimation

Calculation of the absolute backscatter coefficient (BSC), the differential scattering cross

section per unit volume at a scattering angle of 180 degrees, follows the method described by Chen et al. [15, 16]. Using a single element ultrasound transducer, pulses are propagated through water and into the material of interest, and the spectrum of the received backscattered signal voltage determines the BSC after correcting for characteristics of the transducer, instrumentation properties, and ultrasonic properties of intervening materials.

$$BSC(f) \approx \frac{\langle V_g(f) V_g^*(f) \rangle}{C^2 \|T(f) B_0(f)\|^2 \int\int\int \|A(\mathbf{r}, f)\|^4 d\mathbf{r}}$$

Eqn. 6.9

The backscattered signal V_g's spectrum is averaged from many uncorrelated locations in the phantom to obtain the power spectrum. The term C is a constant that accounts for windowing of the signal, and is 0.63 for the Hamming Window. $A(r,f)$ is the complex superposition coefficient determined by the geometric properties of the transducer. A planar reflector is then used to determine $T(f)\ B_0(f)$, where $T(f)$ represents the complex transfer function of the transducer, and $B_0(f)$ is the complex superposition coefficient for the uniform monopole radiator assumed to exist on the transducer surface [16].

6.4.1 Generation of spectra

The transducer used for backscatter analysis was the 710B on a Vevo 770 scanning system (VisualSonics, Inc., Toronto, Canada). Further details on the methods used to adapt the Vevo 770 for quantitative ultrasound imaging research can be found in Appendix A. This transducer has a center frequency of about 25 MHz, and a broad bandwidth, 82% fractional bandwidth at -6dB, as illustrated in Fig. 6.11. The transducer active element is a spherical cap with a projected aperture of 3.5 mm and 15.0 mm radius of curvature. The received signal was digitized at 420

MS/s with 12 bit precision.

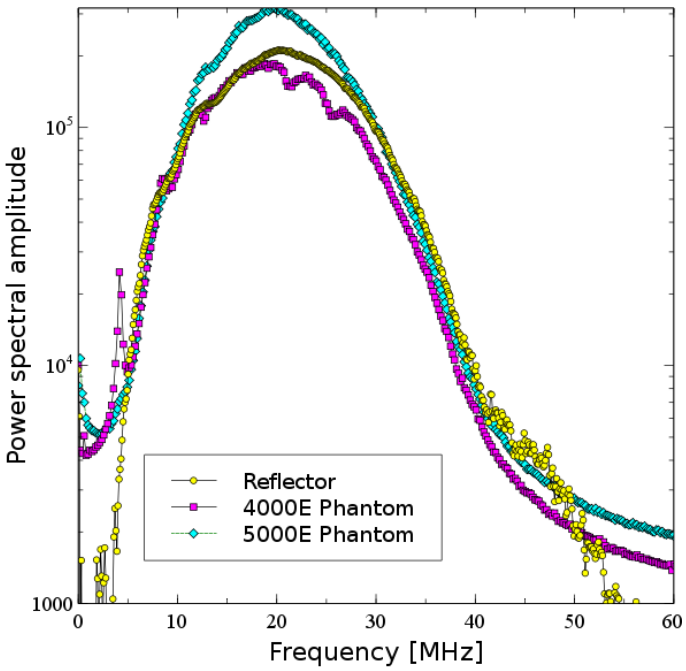

Figure 6.11: Power spectrum derived from radiofrequency data acquired using the 710B transducer for the planar reflector and TM phantoms taken at 10% transmit power.

The Vevo 770, designed for high frequency imaging of small animal targets, is easily saturated when presented with signal from a strong planar reflector that experiences the relatively weak attenuation of a water path. To prevent saturation, a liquid-liquid interface where the two liquids have closely matched acoustic impedances is used [17]. The interface reported by Hall et al. [17] was recreated, which consists of a brominated hydrocarbon mixture covered by water. The hydrocarbon consisted of 39.018% by weight 1-bromoheptane (99% purity, Acros Organics, New Jersey, USA) and 60.982% by weight 1,6-dibromohexane (97% purity, Aldrich Chemical Co., Milwaukee, WI, USA). The planar amplitude reflector reflection coefficient is 0.0138 [17]. An additional receive gain of -5.0 dB in the planar reflector case relative to the TM

phantom signal gain is still required. The reflector was carefully aligned with a gimbal mount to obtain the highest possible amplitude for the backscattered signal. To prevent non-linear effects, planar reflector and TM phantom signal is collected at 10% transmit power. At 10% power, a reasonable tradeoff is achieved that reduces non-linear effects in the planar reflector signal while leaving sufficient signal-to-noise ratio in the TM phantom signals. At higher transmit powers, harmonics introduce lobes into the spectrum as shown in Fig. 6.12.

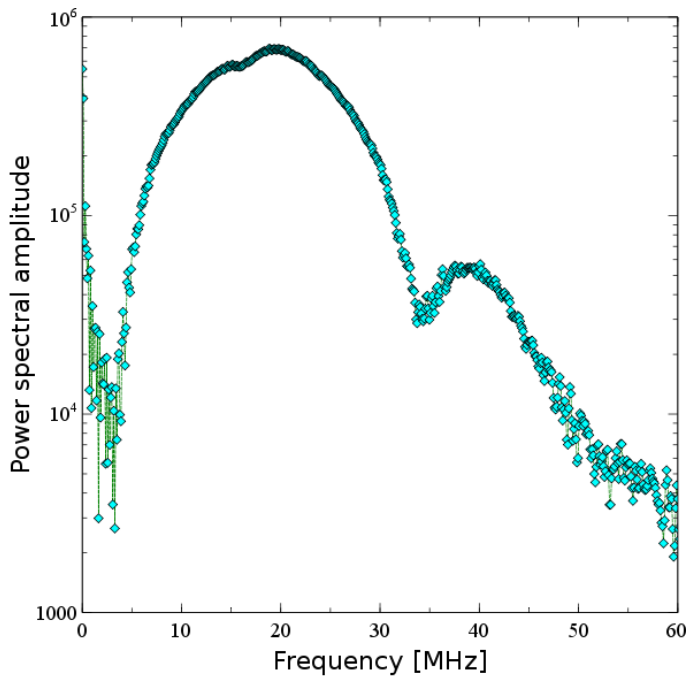

Figure 6.12: Planar reflector spectrum when the 710B transducer is excited at 100% transmit power. Lobes in the upper part of the spectrum are introduced by harmonics generated during non-linear propagation.

The single element transducer can be moved laterally and elevationally, and 1200 independent Fourier spectra of the scattering instances are averaged to obtain the backscattered power spectrum, shown in Fig. 6.11. The 5000E phantom is covered with a thin Saran Wrap® layer as previously described in the substitution experiment, and the 4000E phantom was

covered with a 128 μm-thick TPX® (polymethyl-pentene) layer. A TPX® layer is advantageous relative to a Saran layer because of its low reflection coefficient, which minimizes reverberation effects especially at higher frequencies. The gated window for spectral analysis in the phantom is placed at the focus beyond the surface in an area free from any reverberation artifacts and devoid from the high amplitude response at the surface of the TM phantom. To verify these conditions, data is collected using the online Visualsonics Digital-RF user interface and saved data are utilized for analysis. Sample waveforms from the gate used in calculation of the phantom spectra are shown in Fig. 6.13a) and b). The reflection waveform from the reference planar interface is shown in Fig. 6.13c). Also, screenshots from during acquisition, e.g. Fig. 6.14, demonstrate use of the system's real-time B-Mode display, which is a convenient method to ensure that these conditions are met. Reverberations between the transducer-water interface and the water-phantom interface are a possible source of artifact. These reverberations appear to be present in the Fig. 6.14a) B-Modes images while they are not present in the RF plotted in Fig. 6.14a) nor in Fig. 6.13a). This appears to be is explained by the distinct operation of the Vevo 770 during B-Mode image acquisition and Digital-RF acquisition. For B-Mode acquisition for small animal imaging, the scout-window shown will rotate the transducers at very fast rates to achieve the 200+ frames-per-second required for small animal imaging while continuously transmitting and receiving ultrasound pulses. The reverberation does not have an opportunity to dissipate in this situation. On the other hand, Digital-RF operation is closer to M-Mode data collection; the positioning of the transducer is much slower, and the reverberations are not present in the received signal. In the B-Mode and RF we note the presence of larger scatterers in the 4000E phantom relative to the 5000E phantom, which is consistent with the diameter distribution shown in Fig. 6.1.

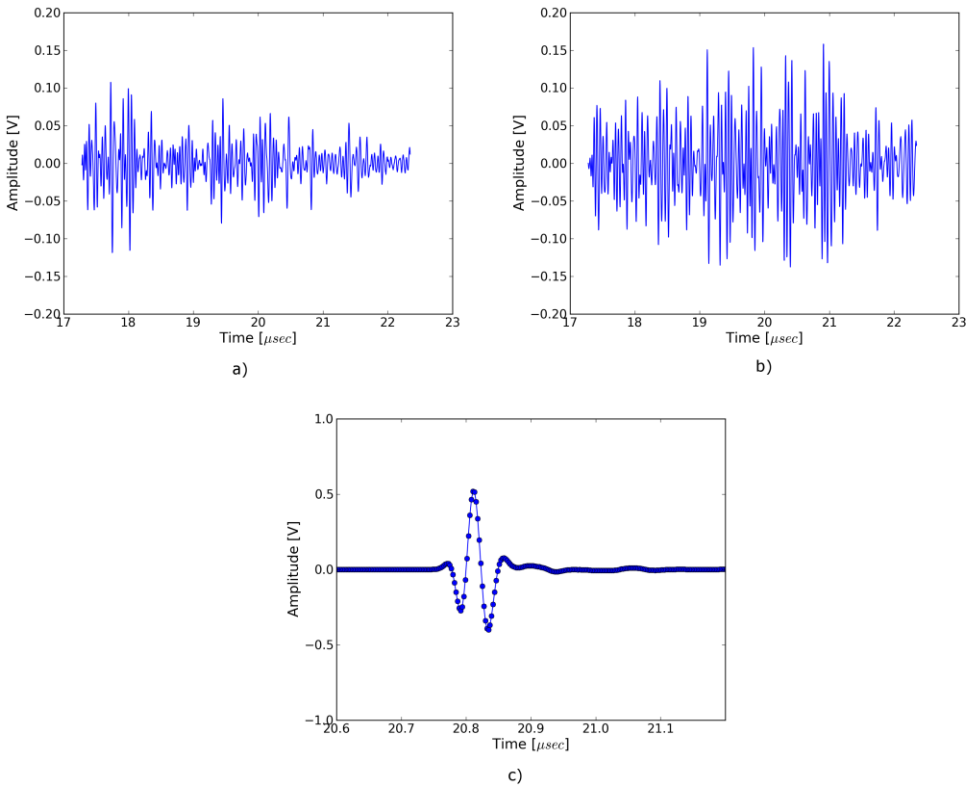

Figure 6.13: Waveforms from the a) 4000E and b) 5000E phantom around the focal region along with c) the planar reflector waveform.

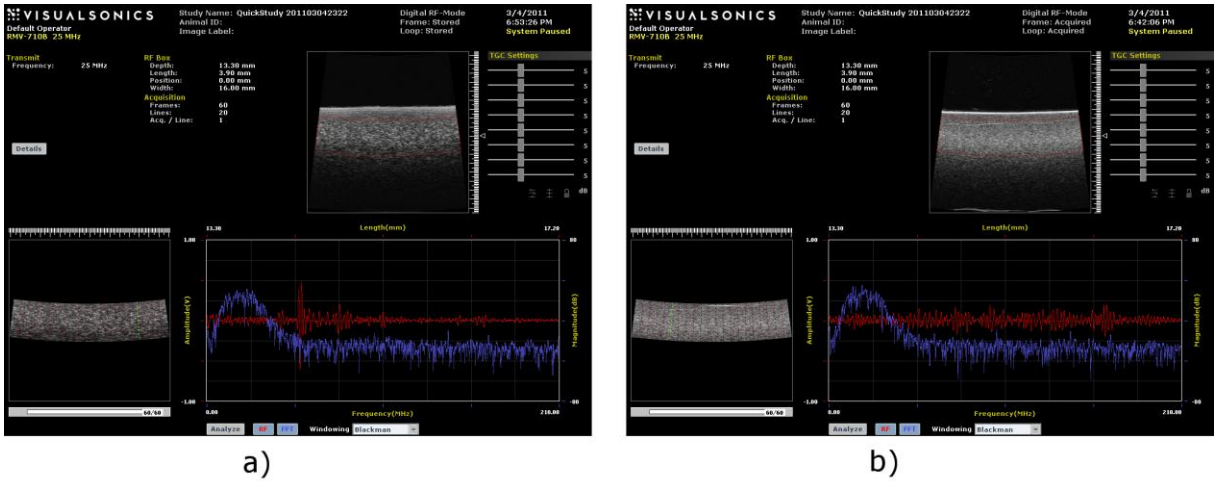

Figure 6.14: Screenshots in Digital-RF mode on the Vevo 770 when collecting phantom data from the a) 4000E and b) 5000E phantoms.

6.4.2 Faran scattering model

Measured BSC are compared to those predicted by the theoretical model of Faran [18]. The medium density is 1.045 g/mL and 1.062 g/mL, respectively, and the glass bead longitudinal speed of sound is 5572 m/s, with a density of 2.380 g/mL and shear wave speed of 3376 m/s. The bead mass per volume phantom is 6.0 kg/m^3 and 15.6 kg/m^3 for the 4000E and 5000E phantom, respectively. Superposition using the diameter distribution given in Fig. 6.1 is assumed. The total mass of the diameter distribution, m_g, is

$$m_g = \rho_m \sum_{i=1}^{N} \frac{\pi}{6} D_i^3 g(D_i), \qquad D_1 = 0,\ D_N = D_{max}$$

Eqn. 6.10

where ρ_m is the bead mass density, D is the diameter of the bead, and $g(D)$ is the diameter distribution. Next, the bead number density - the number of beads of a given diameter per unit volume - is calculated. The bead number density, $\rho_n(D)$, is

$$\rho_n(D) = \frac{\rho_V}{m_g} g(D)$$

Eqn. 6.11

where ρ_V is the bead concentration (mass per unit volume). The backscatter coefficient, a function of frequency f, results from summing the backscatter for a single bead, $BS_s(f,D)$ multiplied by the bead number density,

$$BSC(f) = \sum_{i=1}^{N} BS_s(f, D_i)\rho_n(D_i)$$

Eqn. 6.12

The amplitude attenuation coefficient of the thin layer covering the phantom is assumed to take the form

$$\alpha(f) = \alpha_0 \, f^n$$

Eqn. 6.13

where α_0 = 2.26 Np/m/MHz$^{1.285}$ and n = 1.285 for the 4000E TM phantom α_0 = 5.0 Np/m/MHz$^{1.5}$ and n = 1.5 in the 5000E case.

6.4.3 Backscatter coefficient results

Variations in the BSC versus frequency from both phantoms are displayed in Fig. 6.15. Since the spectral plots in Fig. 6.11 suggested there may be sufficient signal-to-noise ratio up to 45 MHz, analysis is displayed over the entire range from 0 to 50 MHz. There are significant differences between the two phantoms' BSC's, which are amplified at high frequencies. This relationship is observed in both the Faran calculation and reference reflector results. Differences in the predicted BSC of the Faran calculation results are much greater in the 15-30 MHz range than the 5-15 MHz range. The linear slope in the log-log graph with a slope near four indicates Rayleigh scattering in the 6-15 MHz range. Power law regression to the experimental data results in a slope of 3.76 and a coefficient of determination, R^2, of 0.997 for the 5000E phantom. This is expected more for the 5000E phantom because of the smaller bead diameter distribution

evident in Fig. 6.1.

The lower BSC of the 4000E phantom may explain the noisier appearance of the curve, although the dips at 21 MHz and 25.5 MHz are consistently observed with other sets of TM phantom and planar reflector data (not shown). The general trend of the 4000E reference reflector BSC appears to be correct, although there are some oscillations not found in the Faran calculation curve. The reference reflector BSC values are higher in the 5-35 MHz frequency range before converging with the Faran calculation. The mean and standard deviation of the absolute percent difference of the 4000E reference reflector values from the Faran calculation values from 5-50 MHz are 53.6% ± 44.8. Agreement between the Faran calculation and reference reflector results for the 5000E is very close in the 5-15 MHz frequency range. The reference reflector BSC values are higher from 15-35 MHz before also converging again. The mean and standard deviation of the absolute percent difference of the 5000E reference reflector values from the Faran calculation values from 5-50 MHz are 46.6% ± 27.9.

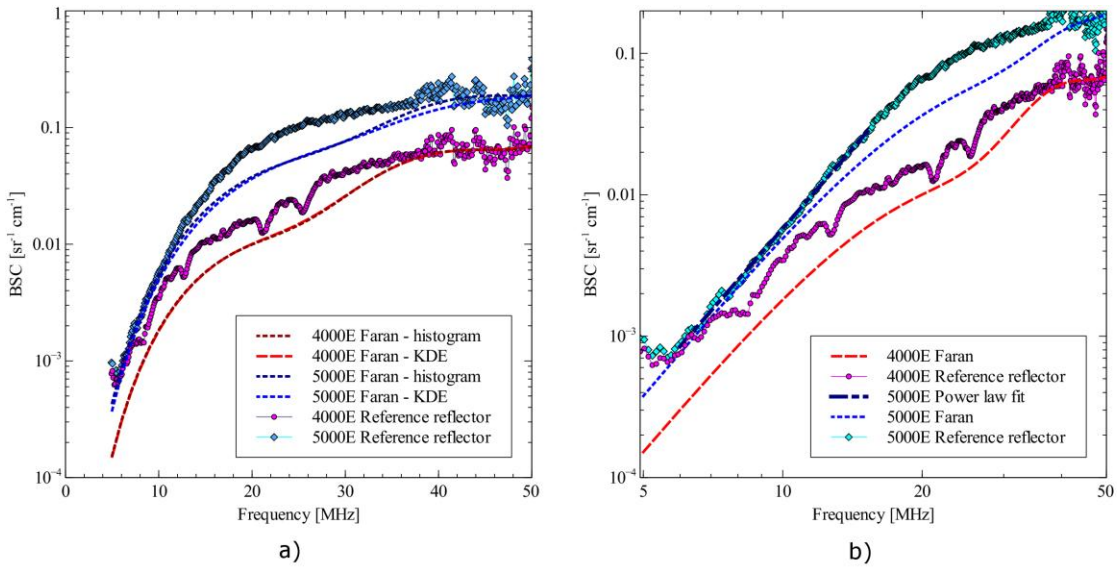

Figure 6.15: Absolute backscatter coefficient for the two TM phantoms examined. A curve derived from the phantom composition and Faran

scattering theory for spherical scatterers is displayed along with results phantom and planar reflector RF data. Dashed lines are the Faran predicted BSC for the acoustic properties assumed for the component materials. Curves with markers represent the experimental results. In a), we present Faran curves for both the histogram approximation of size distribution and the KDE approximation of the size distribution. The same data is present in b), but with logarithmic scaling on both axes. We only plot the KDE Faran curves, but we also show results from power law fit of the 5000E reference reflector data in the 6-15 MHz range.

In this chapter, methods are presented that can be used to measure the absolute backscatter coefficient at high frequencies. Accurate measurement of this quantity has proven difficult for low frequencies [8], and additional challenges caused by alignment and attenuation make it significantly more difficult at high frequencies. There are a number of input parameters and assumptions in the broadband BSC reference reflector calculation that can be sources for error.

Approximation of the acoustic field amplitude in the scattering volume depends on a model of a single element spherical capsule transducer with uniform apodization [16]. The Vevo 770 approximates this configuration. Ideally, the aperture radius and radius of curvature would be empirically determined by acoustic field measurements with a hydrophone. A hydrophone with sufficiently small footprint for the short wavelength encountered was unavailable, so the geometrical properties provided by manufacturer specifications were applied.

Calculation of the BSC also relies on measurement of the sample speed of sound and attenuation coefficient. We saw that high sampling frequencies are required for precise measurement of the speed of sound, and linear interpolation of the zero-crossing can increase the precision of delay measurement. Care has to be taken to prevent offsets in the delay from occurring due to building vibration, inadvertent load on the apparatus by the experimenter, or vibrations of the transducer from water flow from the tank heater. Distortion of the signal at the pulse edges, as shown in Fig. 6.5, makes determination of the phase velocity challenging for

frequencies of 30 MHz or higher. Successful attenuation measurement relies on proper alignment and sufficient signal amplitude. The transducers must be placed close together to prevent excessive signal loss in the water path. This requires precise alignment of the transducers. The TM specimen used for substitution needs to have a small width to prevent signal loss, but this also makes precise width measurement more important. High excitation voltages are required to obtain adequate signal at high frequencies, but these same high voltages cannot also be used at lower frequencies because non-linear propagation will occur in water.

There are three significant differences in the two phantoms examined in this chapter: the thin layer material covering the phantom and the glass bead size distribution and concentration. Incorrect assumptions of the thin layer properties would affect the measured BSC, and incorrect assumptions on the bead distribution density would result in an incorrect Faran calculation.

Kernel density estimation is investigated as a method to improve estimation of the bead diameter distribution, but this was found to have negligible effects on the BSC curves. However, there was a very high sensitivity of the Faran BSC curves to rare, large diameter beads; a large number of diameter measurements were required before reasonable results were obtained. Due to the cubic relationship between diameter and volume, the large diameter beads are significant in the calculation in the total mass of a bead distribution. In turn, this affects the bead number density, which shifts the theoretical BSC curve up or down. The presence of the rare, large scatterers influences the shape of the curve in the non-Rayleigh regions. In practice, it is easier to obtain agreement between experimental and theoretical results when the bead diameter distribution is much smaller than the wavelength (Rayleigh scattering), and the distribution lacks rare outliers.

6.5 References

[1] E. Madsen, G. Frank, M. McCormick and M. Deaner. Anechoic Sphere Phantom for Estimating 3-D Resolution of Very High Frequency Ultrasound Scanners. *IEEE Transactions on Ultrasonics Ferroelectrics and Frequency Control* 57, 2284--2292. 2010.

[2] G. R. Lockwood, L. K. Ryan, J. W. Hunt and F. S. Foster. Measurement of the ultrasonic properties of vascular tissues and blood from 35-65 MHz. *Ultrasound Med Biol* 17, 653--666. 1991.

[3] M. Rosenblatt. Remarks on some nonparametric estimates of a density function. *The Annals of Mathematical Statistics* 27, 832--837. 1956.

[4] E. Parzen. On estimation of a probability density function and mode. *The Annals of Mathematical Statistics* 33, 1065--1076. 1962.

[5] B. W. Silverman. *Monographs on Statistics and Applied Probability: Density estimation for statistics and data analysis*. London: Chapman & Hall/CRC. 1986.

[6] M. Laurel and American Institute of Ultrasound in Medicine Technical Standards Committee. Methods for Specifying Acoustic Properties of Tissue Mimicking Phantoms and Objects. Stage 1. 1995.

[7] E. L. Madsen, F. Dong, G. R. Frank, B. S. Garra, K. A. Wear, T. Wilson, J. A. Zagzebski, H. L. Miller, K. K. Shung, S. H. Wang, E. J. Feleppa, T. Liu, W. D. O'Brien, K. A. Topp, N. T. Sanghvi, A. V. Zaitsev, T. J. Hall, J. B. Fowlkes, O. D. Kripfgans and J. G. Miller. Interlaboratory comparison of ultrasonic backscatter, attenuation, and speed measurements. *J Ultrasound Med* 18, 615--631. 1999.

[8] K. A. Wear, T. A. Stiles, G. R. Frank, E. L. Madsen, F. Cheng, E. J. Feleppa, C. S. Hall, B. S. Kim, P. Lee, W. D. O'Brien, M. L. Oelze, B. I. Raju, K. K. Shung, T. A. Wilson and J. R. Yuan. Interlaboratory comparison of ultrasonic backscatter coefficient measurements from 2 to 9 MHz. *J Ultrasound Med* 24, 1235--1250. 2005.

[9] G. W. C. Kay and L. H. Laby. *Table of Physical and Chemical Constants*. Online: The National Physical Laboratory. 1995.

[10] M. O. Culjat, D. Goldenberg, P. Tewari and R. S. Singh. A review of tissue substitutes for ultrasound imaging. *Ultrasound in Medicine & Biology* 36, 861--73. 2010.

[11] K. A. Wear. Group velocity, phase velocity, and dispersion in human calcaneus in vivo. *The Journal of the Acoustical Society of America* 121, 2431--2437. 2007.

[12] V. A. Del Grosso and C. W. Mader. Speed of Sound in Pure Water. *The Journal of the Acoustical Society of America* 5, 1442--1446. 1972.

[13] K. R. Waters, M. S. Hughes, J. Mobley, G. H. Brandenburger and J. G. Miller. On the applicability of Kramers–Kr"onig relations for ultrasonic attenuation obeying a frequency power law. *The Journal of the Acoustical Society of America* 108, 556. 2000.

[14] J. Mobley, K. R. Waters and Miller. Finite-bandwidth effects on the causal prediction of ultrasonic attenuation of the power-law form. *The Journal of the Acoustical Society of America* 114, 2782. 2003.

[15] J. F. Chen, J. A. Zagzebski and E. L. Madsen. Tests of backscatter coefficient measurement using broadband pulses. *IEEE Transactions on Ultrasonics Ferroelectrics Frequency Control* 40, 603--7. 1993.

[16] E. L. Madsen, M. F. Insana and J. A. Zagzebski. Method of data reduction for accurate determination of acoustic backscatter coefficients. *The Journal of the Acoustical Society of America* 76, 913--923. 1984.

[17] T. J. Hall, E. L. Madsen, F. Dong, I. R. Medina and G. R. Frank. Low-reflection-coefficient liquid interfaces for system characterization. *Ultrasound in Medicine and Biology* 27, 1003--1010. 2001.

[18] J. J. Faran. Sound scattering by solid cylinders and spheres. *The Journal of the Acoustical Society of America* 23, 405--418. 1951.